


## RESEARCH ARTICLE OPEN ACCESS

# Characterizing the Atmospheric Boundary Layer for Offshore Wind Energy Using Synthetic Aperture Radar Imagery

Justin E. Stopa<sup>1</sup>  | Doug Vandemark<sup>2</sup> | Ralph Foster<sup>3</sup> | Marc Emond<sup>2</sup> | Alexis Mouche<sup>4</sup> | Bertrand Chapron<sup>4</sup>

<sup>1</sup>Department of Ocean Resources and Engineering, The School of Ocean and Earth Science and Technology, The University of Hawai'i at Mānoa, Honolulu, Hawai'i, USA | <sup>2</sup>Ocean Processes Analysis Laboratory, The University of New Hampshire, Durham, New Hampshire, USA | <sup>3</sup>Applied Physics Laboratory, The University of Washington, Seattle, Washington, USA | <sup>4</sup>Laboratoire d'Océanographie Physique et Spatiale (LOPS), Univ. Brest, CNRS, IRD, Ifremer, IUEM, Bretagne, France

**Correspondence:** Justin E. Stopa ([stopa@hawaii.edu](mailto:stopa@hawaii.edu))

**Received:** 18 July 2023 | **Revised:** 16 May 2024 | **Accepted:** 20 May 2024

**Funding:** R.F. and D.V. were supported by NASA Physical Oceanography through grants NNX17AH17G and 80NSSC20K0822. The latter NASA grant, 80NSSC20K0822, and grant number 2132150 from the National Science Foundation supported J.S. and is referenced by the School of Ocean and Earth Science and Technology (SOEST) contribution number 11822. A.M. was supported by ESA Contract No. 4000135827/21/NL - Harmony Science Data Utilisation and Impact Study for Ocean. A.M. and B.C. were also supported by ESA Sentinel-1 Mission Performance Center 465 (4000107360/12/I-LG). We thank ESA for providing the data and IFREMER for the computing resources used in this study.

**Keywords:** atmospheric boundary layer | offshore wind energy | synthetic aperture radar | wind energy assessment

## ABSTRACT

Measuring boundary layer stratification, wind shear, and turbulence remains challenging for wind resource assessment. In particular, larger eddy scales have the greatest impact on turbine load fluctuations, and there are few in situ methods to observe them adequately. Satellite remote sensing using synthetic aperture radar (SAR) is an alternative approach. In this study, eddy-related signatures in 704 high-resolution images are related to stratification through a bulk Richardson number ( $Ri$ ) measured by a buoy near Martha's Vineyard, the US epicenter of offshore wind. Variations in SAR-observed atmospheric boundary layer eddies, or lack of them, correspond to specific  $Ri$  regimes. Accounting for strong vertical wind shear, typically under stable stratification, is critical for energy production and turbine loads, and SAR directly identifies these conditions by the absence of energetic eddies. SAR also provides a regional climatology of atmospheric stratification for offshore wind assessment, complementing other observations, and with potential application worldwide.

## 1 | Introduction

One challenge for offshore wind energy production is to characterize, monitor, and predict wind dynamics within the marine atmospheric boundary layer (MABL). Shaw et al. [1] review these offshore wind resource measurement challenges and highlight the importance of determining and accounting for changes in boundary layer stratification, wind shear, and turbulence. They find that few datasets provide these quantities at the needed spatial and temporal coverages and that field measurement options are limited or do not yet exist. This is partially due to logistical

and cost-prohibitive aspects of operating a long-term array of vertically resolving wind and thermal profilers in an offshore environment. Satellite remote sensing is one alternative approach to address the issue, and synthetic aperture radar (SAR) has already been used, often in tandem with satellite wind scatterometers, to map surface wind variability at a very high spatial resolution near existing and candidate wind generation sites [2–5]. SAR has been used to observe and study the turbulent wakes within a wind farm [6]. Additionally, SAR measurements of sea surface roughness have been extrapolated to wind speeds at turbine heights ( $\approx 80$  m) above the sea surface [7–9].

This is an open access article under the terms of the [Creative Commons Attribution-NonCommercial](https://creativecommons.org/licenses/by-nc/4.0/) License, which permits use, distribution and reproduction in any medium, provided the original work is properly cited and is not used for commercial purposes.

© 2024 The Author(s). *Wind Energy* published by John Wiley & Sons Ltd.

While remote sensing of surface wind vectors and their spatial variability has a clear value, it provides no direct information on boundary layer stratification, vertical wind shear, or turbulence. An ocean SAR remote sensing approach to estimate surface stratification [10] objectively provides surface layer stratification and km-scale wind coherence data complementing in situ wind, wind profiler, and satellite surface wind observations used in wind energy resource assessment. The approach stems from the well-known SAR capability to resolve coherent structures of scale 0.5–5 km [11–13] that span the boundary layer and induce modulation to the sea surface roughness that SAR can measure.

Stopa et al. [10] showed that SAR detection of different coherent structure types corresponds to particular surface layer stratification regimes providing a capability to delineate between unstable, near-neutral, and stable boundary layers. The surface stratification was characterized using a bulk Richardson number [14] calculated from the ERA5 surface analyses [15]. The current study includes a direct comparison with in situ data to further assess those findings.

The atmospheric stratification directly relates to the wind elevation profile or shear [16]. The organized large eddies ( $L > 500$  m and  $t > 1$  min) influence load fluctuations [1]. The SAR measurements of energetic eddies of 0.5–5 km are the focus of this work. The upper limit of 5 km is partially due to the 20-km footprint of

Sentinel-1 (S-1) wave mode (WV). This remote sensing approach of extracting information from SAR textures might benefit offshore wind resource assessments.

The chosen study region is a focal point of wind resource development—southwest of Martha's Vineyard (see Figure 1). This allows us to use several long-term in situ studies of surface layer stratification, vertical wind shear, their correlation, and implications for wind dynamics at turbine heights of 50–80 m [16–18]. The Gulf Stream, a western boundary current, influences this location by transporting warm water from the south (see the sea surface temperatures in Figure 1). The region is also home to the first US offshore wind energy projects including the Block Island Wind Farm, which has a capacity of 30 MW [19], the Coastal Virginia Offshore Wind (12 MW), and at least six more projects coming online in the next 2 years. The study site has regional satellite SAR coverage provided by the European Space Agency's S-1 satellites. S-1 covers 7 years (2016–2022), and this period overlaps with long-term surface observations collected by the offshore Ocean Observatories Initiative Coastal Pioneer Array (CPA) (70.88° W, 40.1° N) [20].

Several recent in situ studies have addressed boundary layer properties as they relate to wind turbine operation in this region [16–18]. These studies provide a useful backdrop for the present remote sensing investigation. In particular, their work details seasonality and spatial variability in vertical shear and

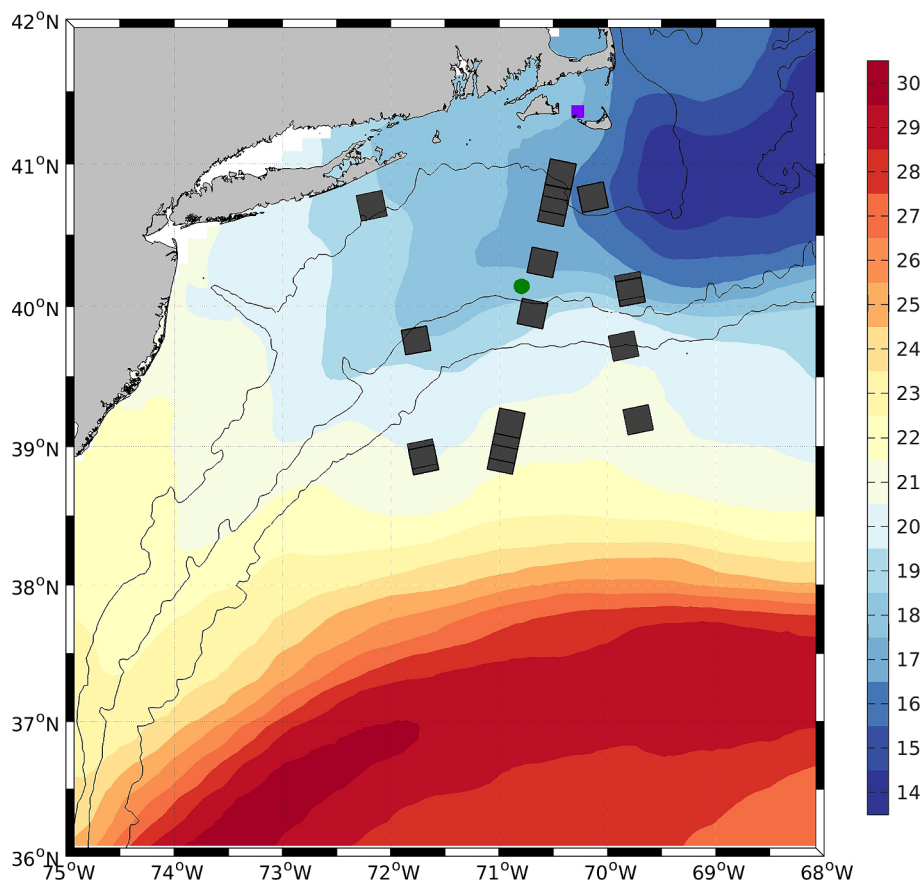


**FIGURE 1** | Site location of the Coastal Pioneer Array (green circle) and the Air-Sea Interaction Tower (ASIT) (purple square) in the NW Atlantic Ocean. The gray squares denote the S-1 acquisitions. The colors denote the average sea surface temperature for June 2017 in degrees Celsius derived from passive radiometers.

stratification conditions, where unstable and stable boundary layers (SBLs) are frequently observed due to numerous effects including strong ocean temperature gradients, atmospheric transitions near the coasts, and synoptic-scale systems.

This study uses 704 S-1 SAR WV images surrounding the CPA central buoy mooring from 2016 to 2022 to assess the boundary layer stratification. The atmospheric and oceanic features in each image are classified by visual inspection based on the definitions given in [21, 22]. The image textures observed in the SAR imagery are related to a bulk Richardson number. One goal in comparing these results to previous regional assessments is to determine the potential for wider use of SAR data to support offshore wind development needs [23]. The methods, results, discussion, and conclusions are given in Sections 2, 3, 4, and 5, respectively.

## 2 | Methods and Datasets

Table 1 summarizes the key abbreviations used in this study.

The highest resolution SAR imaging mode from S-1 is the WV. The WV is used throughout this work. S-1 WV images with  $20 \times 20$  km footprints were visually examined to detect textural signatures associated with 12 separate phenomena: negligible atmospheric variability (NV), wind streaks (WS), micro-scale convection (MC), atmospheric gravity waves (AW), atmospheric or gust front (AF), cold pools or rain cells (RC), biological slicks (BS), internal ocean gravity waves (IW), ocean fronts (OF), low wind region (LW), and as an undefined atmosphere or ocean (UD). Next, a consensus among the multiple independent visual labels was determined by re-evaluating each image and the independent tags. The consensus label was used throughout this work. Each image is multi-labeled—meaning each image might contain more than one of the 12 labels. Representative examples of the 12 SAR classes are shown in Figure 2. Only the S-1B satellite, launched in May 2016 in orbit  $180^\circ$  apart from S-1A but in the same orbital plane, collects data within the bounds of our study site. Various subsets of the 704 images are used throughout the manuscript. Only 30 images are centered within a 75-km radius of the CPA buoy. Most images lie between 75 and 98 km away from this central location. These large spatial differences are assessed using the time variations measured at the buoy and are described below.

Data from the CPA buoy are quality-controlled using flags provided by the Ocean Observatories Initiative [20]. Furthermore, suspect data are replaced with data from the redundant sensors when available. CPA became operational in December 2014, and there have been six main deployments throughout the period coinciding with the S-1 acquisitions. The time series ends in December of 2021 when S-1B became inoperable. There are approximately seven full years of data with some missing periods. Most CPA sensors collect data at 1- to 10-min intervals. Some anemometers measure wind speeds in three dimensions at 4.85 and 4.74 m above the sea surface.

One measure of MABL surface layer stratification is a bulk Richardson number:

**TABLE 1** | Abbreviations used in this paper.

Abbreviation	Meaning
AF	SAR texture of an atmospheric or gust front
AW	SAR texture of atmospheric gravity waves
BS	SAR texture of biological slicks
CPA	Coastal pioneer array—moored buoy
DJF	December–January–February
IW	SAR texture of internal ocean gravity waves
JJA	June–July–August
LW	SAR texture of low winds
MABL	Marine atmospheric boundary layer
MC	SAR texture of cells or micro-scale convection observed as a popcorn-like pattern
NNBL	Near-neutral boundary layer—derived from buoy Ri
NV	SAR texture defined by the lack of rolls or cells
OF	SAR texture of ocean fronts
RC	SAR texture of rain cells
Ri	Richardson number—buoyancy/shear
S-1	Sentinel-1—the European Space Agency's SAR mission
SAR	Synthetic aperture radar
SBL	Stable boundary layer—derived from buoy Ri
UBL	Unstable boundary layer—derived from buoy Ri
UD	SAR texture of unidentified ocean of atmosphere features
WS	SAR texture of atmospheric rolls or wind streaks - observed as a streaky pattern
WV	Wave mode—open ocean S-1 imaging mode

$$Ri = \frac{g}{T_{10v}} \frac{z_{10}(T_{10v} - SST_v)}{U_{10}^2} \quad (1)$$

where  $g$  is the acceleration due to gravity,  $U_{10}$  is the wind speed at  $z_{10} = 10$  m above the sea surface, and  $T_{10v}$  is the virtual temperature at  $z_{10}$ . CPA buoy wind speeds are collected at a height of 4.85 m, and they are converted to 10 m using COARE [24].  $T_{10v}$  is the virtual air temperature and includes the effects of moisture on the air density. CPA measures the necessary scalar quantities to estimate the bulk  $Ri$ . The air temperature, humidity, and pressure data are collected 4.25 m from the ocean surface.



Wind speeds are regularly estimated from the SAR using geophysical model functions. The input of the geophysical model functions include the radar cross-section, wind direction, and polarization. We use CMOD5N [25] to estimate the wind speeds from SAR at the standard height of 10 m from the surface with neutral stratification using the measured radar cross-section and wind directions estimated from the SAR imagery [26].

### 3 | Results

#### 3.1 | SAR Textures to Atmospheric Stratification

Example SAR sea surface roughness images are shown in Figure 2. This work is built on two main findings from previous works. The first is that SAR captures MABL coherent structures by relating the km-scale sea surface roughness to organized wind field fluctuations [11, 12, 27–30]. The second point is that varied coherent structures (like rolls and cells) are strongly related to local stratification [31–33]. When the

production of turbulence due to buoyancy is significantly larger than that due to shear, the MABL stratification is unstable, and the turbulence is convective. An unstable MABL generates cellular coherent structures that span the MABL depth, or at least the sub-cloud layer, called micro-scale cells (MC). The near-surface circulation of the MC locally perturbs the surface wind stress and induces a nominally hexagonal pattern on the sea surface roughness (Figure 2d). When the production of turbulence by shear is significantly larger than the buoyancy flux, the stratification is near-neutral, and roll vortices are generated and span the MABL depth and roughly align with the mean wind direction. The rolls induce parallel bands of locally enhanced or reduced surface wind stress imprint on the sea surface roughness. We reference these SAR textures as rolls or WS (Figure 2b). WS can form in weakly stable stratification since they are induced by shear [34]. When the stratification lies between these two regimes, both linear features of WSs and the cellular structures (MC) are observed; an example of forced convection (WS/MC) or a combination of rolls and cells is in Figure 2c. In the less common condition where the near-surface virtual temperature is larger than that

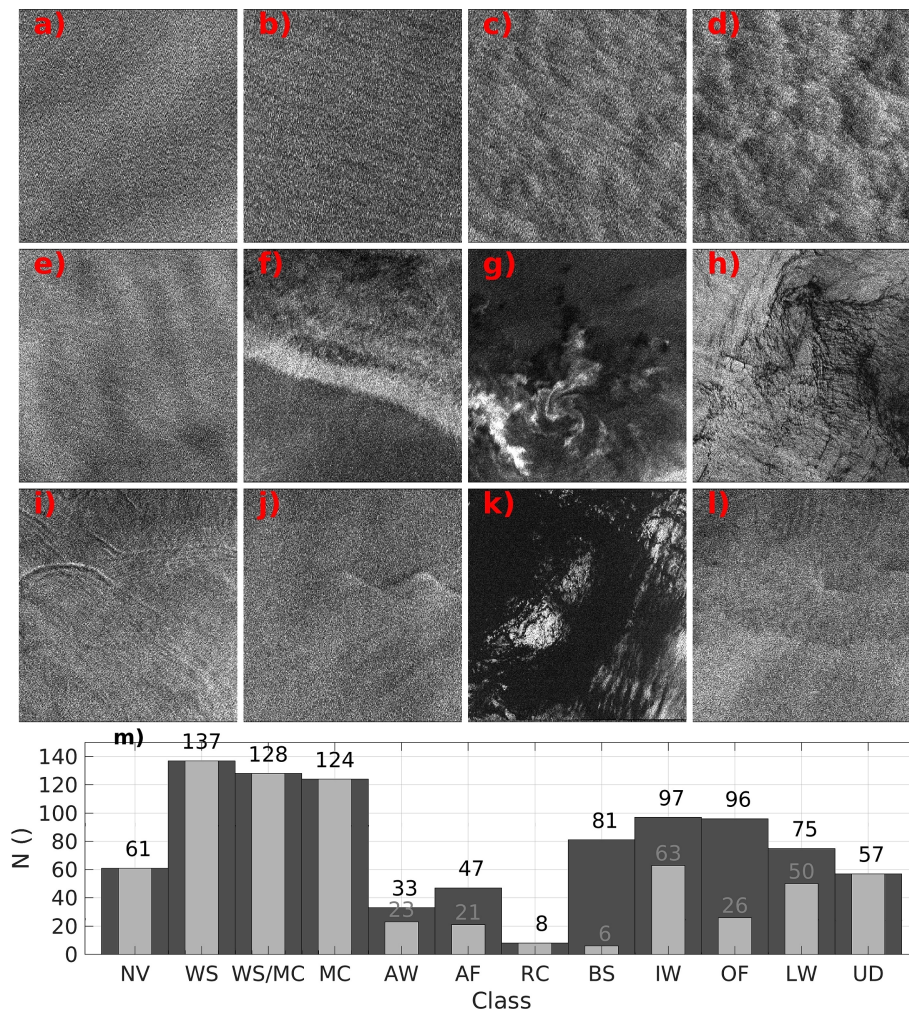


**FIGURE 2** | Twelve representative examples of the geophysical phenomena observed at the CPA in the NW Atlantic: negligible atmospheric variability (NV) (a), wind streaks (WS) (b), a mixture of WS and micro-scale cells (MC) (c), MC (d), atmospheric gravity waves (AW) (e), atmospheric or gust front (AF) (f), rain cells (RC) (g), biological slicks (BS) (h), internal ocean gravity waves (IW) (j), ocean front (OF) (j), low wind region (LW) (k), and unidentified ocean or atmosphere (UD) (l). The bar plot in (m) shows the number of images for each category. All images are multi-tagged and the dark bars represent the total number of tags for each class. The light gray bars represent the dominant class for each image of the 704 images.



of the sea surface, the buoyancy flux is downward  $Ri > 0$ , and the MABL is stably stratified. Above a small  $Ri$  threshold, both rolls (WS) and cells (MC) are suppressed, and we refer to this texture as NV (Figure 2a). NV, WS, and MC refer to textures observed in SAR imagery, and these classes were shown to respectively correspond to  $Ri$  ranges associated with stable, near-neutral, and unstable stratification states [10].

The SAR textures in Figure 2 have all been long-observed in SAR imagery, and a description can be found in [21]. More details of 10 common classes observed in S-1 WV global imagery are provided in [22]. NV, WS, WS/MC, and MC (top row of Figure 2) are the most common classes that account for 65% of the database. Eight other observed classes have distinct ocean or atmosphere signatures and are summarized here. AW (Figure 2e) have distinct linear features that typically have larger scales than rolls (WS), and the wavefronts are perpendicular to the wind direction. Atmospheric fronts (AF) or gust fronts (Figure 2f) often have a distinct linear or curved feature with a bright-dark contrast in sea surface roughness. RC (Figure 2g) contain isolated bright spots surrounded by dark regions. BS (Figure 2h) are defined by multiple dark linear and curved features where surface surfactants have converged to suppress wind-induced surface roughness. Internal ocean waves (IW) (Figure 2i) have distinct wave fronts that are often well-defined as linear or slightly curved features. OF (Figure 2j) appear as bright linear or meandering features and represent boundaries between water masses that can be caused by differences in temperature, salinity, or density. OF often coexist with other phenomena. LW (Figure 2k) images are defined as having a strong contrast between dark and bright areas over large portions of the image and have more pronounced ocean wave signatures with weaker wind speeds ( $< 3 \text{ m s}^{-1}$ ). Lastly, undefined (UD) (Figure 2l) images contain either ocean or atmosphere features that are difficult to classify. In this case, the geophysical features inducing the SAR roughness variations often have larger scales than the 20-km footprint. In total, 87% of the images have dominant features related to atmospheric impacts while 13% relate to the ocean. SAR images dominated by atmospheric signatures might also contain less pronounced ocean signatures like OF.

Each satellite image is referenced to the closest-in-time CPA buoy measurement. Due to data outages and maintenance, there are 550 S-1/CPA matches. However, some of the matches have relatively large distances exceeding 100 km. The MABL stratification is driven by the ocean modulations of the Gulf Stream and passing atmospheric baroclinic storms. Both can produce large spatial gradients in air-sea temperature differences and wind speeds across the  $> 100 \text{ km}$  distances between the moored buoy and the SAR acquisition. To mitigate the effects of the large spatial differences, we used the standard deviation of the wind direction 3h preceding the SAR overpass as an indicator of the spatial variability. When the standard deviation of the wind direction is less than  $20^\circ$ , we assume that the region is not drastically changing in space, and the SAR image is likely representative of the buoy observations. Using this criterion left 420 images for the buoy S-1 comparison. Figures 3 and 4 are based on these 420 images.

The relationship between the SAR image class and bulk  $Ri$  is given in Figure 3. Overall, the MABL is stable for NV ( $Ri > 0$ ),

near-neutral for rolls (WS) ( $Ri \in [-0.008, 0.007]$ ), and unstable for cells (WS/MC and MC) ( $Ri < 0$ ). The correspondence of the SAR textures NV, WS, WS/MC, and MC with distinct  $Ri$  regimes is consistent with the global comparison of S-1 imagery with  $Ri$  derived from ERA5 [10]. During BOMEX, [35] analyzed data from direct aircraft turbulence measurements and showed that the MABL underwent a major state change from rolls to cells across a narrow stratification range. Based on this limited dataset, Grossman [35] proposed a transition from pure rolls (WS) to pure cells (MC) through a set of intermediate classes in which both cells and rolls were present. Figure 3 shows the continuum of SAR classes: NV, WS, and WS/MC and MC maps to positive, close to zero, and negative Richardson numbers confirming Grossman's hypothesis in a different environment—the extra-tropics. These results complement the [10] study by confirming that the relationship between SAR textures and stratification holds when compared to in situ observations in the Northwest Atlantic.

The  $Ri$  inter-quartile ranges for each class are given in Table 1. The  $Ri$  regimes for rolls (WS) and mixed rolls and cells (WS/MC) are significantly different because the inter-quartile ranges do not overlap. On the other hand, the roll/cell (WS/MC) and cell (MC) textures' inter-quartile range have significant overlap; suggesting these classes occupy the same  $Ri$  regime. Thus, while stratification plays a leading role in the MABL roll dynamics, other factors such as the mean shear profiles are also important. Cells (MC) are slightly more unstable with a median of  $Ri = -0.028$  compared to the mixed rolls and cells (WS/MC) median of  $Ri = -0.022$ . The coexistence of rolls and cells in unstable MABL is consistent with previous investigations [27, 35, 36].

Inspection of all imagery collected in the region alongside the buoy-derived stratification data led to the realization that, at least in this NW Atlantic region, several other observed SAR phenomena also routinely map into specific stratification regimes. This extends the SAR stratification mapping methods beyond that of Stopa et al. [10] as illustrated here in Figure 3 and Table 2. For example, AW correspond to SBLs, which is expected because their formation requires stable stratification. Atmospheric fronts (AF) have a stable or near-neutral MABL. RC are typically characterized by strong convection, but these six images unexpectedly map to stable  $Ri$ . RC are highly localized, and the correlation across the  $\approx 100 \text{ km}$  distance between the satellite and buoy is likely poor. BS correspond to stable stratification, and these textures often coexist with other phenomena like LW, IW, or OF. IW images correspond to stable MABL. OF and LW images span the entire  $Ri$  range, meaning they are not strong indicators of atmospheric stratification. The  $Ri$  of the LW class spans the entire range ( $\pm 0.2$ ) and is consistent with previous works suggesting that wind-induced surface roughness occurs above a threshold near  $U_{10} > 3 \text{ m s}^{-1}$  detected by SAR [37]. In summary,

- forced convective states (WS/MC and MC) represent unstable boundary layers (UBLs)
- rolls (WS) and atmospheric fronts (AF) represent near-neutral boundary layers (NNBLs)
- NV, AW, and internal waves (IW) represent SBLs

and these SAR textures can be used as indicators of MABL stratification regimes. On the other hand, RC, BS, LW, and

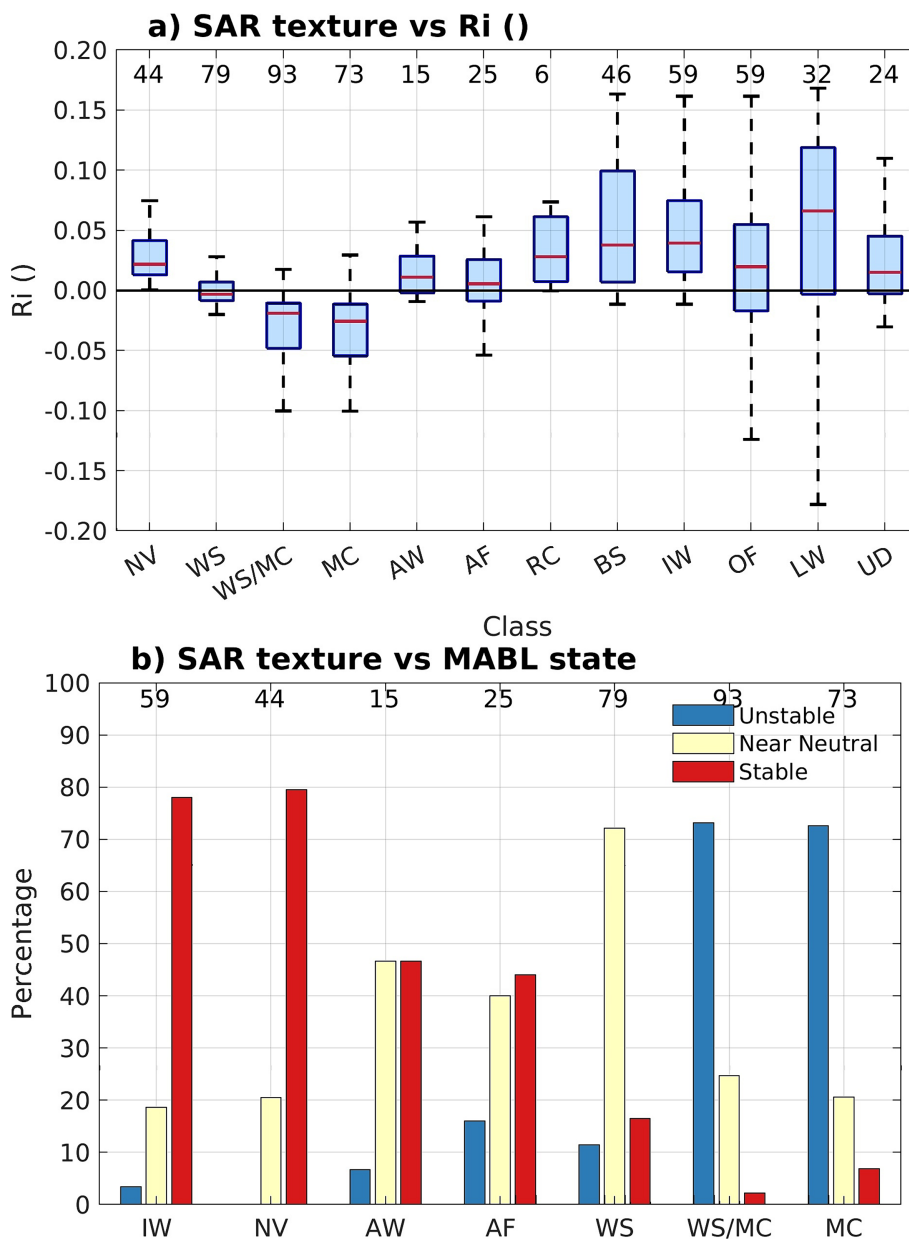


**FIGURE 3** | Box and whisker plot (a) showing the relationship between the labeled S-1 images and  $Ri$ . The box represents the middle 50% of the data or inter-quartile range, the red horizontal lines are the median, and the black dashed lines represent 99% of the data using  $\pm 2.7 \times$  the standard deviation. The SAR hand-labeled classification versus a stratification classification based on buoy stratification regions based on  $Ri$  (b). The number of images is given on the top of the panel.

unidentified (UD) classes are either under-sampled (RC), not well-linked to specific  $Ri$  ranges (BS or LW), or undefined (UD). These four classes are not further analyzed.

The  $Ri$  inter-quartile ranges and standard deviations are given in Table 2. Figure 3a and Table 2 show that when cells are present (WS/MC or pure MC), the images correspond to a larger  $Ri$  range relative to pure WS or NV. Pure rolls (WS) have the smallest standard deviation of any class, and while commonly observed, they reside only in a narrow niche of near-neutral stratification centered near  $Ri = -0.003$ . This emphasizes that MABL WS are associated with shear instabilities [38]. The NV, AW, and IW classes align with SBLs (negative buoyancy;  $Ri > 0$ ). Conversely, the WS/MC and MC classes are UBLs and occur when there is positive buoyancy or less dense air rising ( $Ri < 0$ ). When

buoyancy nears zero, WS predominate over other classes, and there is an NNBL.

The S-1/buoy match-ups can define a categorical classification of the MABL stratification based on  $Ri$ . The NV P25, AW P25, internal wave (IW) P25, atmospheric front (AF) P75, and WS P75 are averaged to make a distinction between stable and NNBLs. The atmospheric front (AF) P25, WS P25, WS/MC P75, and MC P75 are averaged to make a distinction between near-neutral and UBLs. The 3-state MABL stratification classification is as follows:

- UBL:  $Ri < -0.010$
- NNBL:  $-0.010 \leq Ri \leq 0.011$
- SBL:  $Ri > 0.011$ .

**TABLE 2** | *Ri* inter-quartile ranges for the different SAR classes where P25, P50, and P75 denote the 25th, 50th (median), and 75 percentiles, respectively.

SAR Class	MABL Class	P25	P50	P75	STD
IW	SBL	+0.016	+0.040	+0.075	0.122
NV	SBL	+0.013	+0.022	+0.041	0.057
AW	SBL	-0.002	+0.011	+0.029	0.065
AF	NNBL	-0.009	+0.006	+0.026	0.067
WS	NNBL	-0.008	-0.003	+0.007	0.031
WS/MC	UBL	-0.048	-0.019	-0.011	0.044
MC	UBL	-0.054	-0.026	-0.011	0.060

Note: The MABL classes are approximate and based on the *Ri* ranges typical for a stable boundary layer (SBL), near-neutral boundary layer (NNBL), and unstable boundary layer (UBL).

Figure 3b demonstrates the relationship between the SAR textures and the categorical MABL state based on buoy bulk *Ri*. Internal wave (IW) images are mostly found in SBLs (82%). This is likely because we only observe internal waves (IW) in SAR imagery when atmospheric phenomena like rolls, cells, fronts, or rain (WS, MC, AF, RC, ...) are not strongly influencing the ocean surface roughness. Negligible atmospheric variability (NV) textures correspond to SBLs (80%) consistent with [10]. The presence of an AW signature at the sea surface implies stable stratification ( $Ri > 0$ ). Stable stratification is generally less common over the ocean, and a point measurement is unlikely to characterize its presence over the larger study area. SAR has an advantage by being able to capture large spatial expanses.

Only a portion, 17%, of the atmospheric front (AF) images are associated with UBLs, and the images occasionally contain cellular signatures consistent with convection. Otherwise, the atmospheric front (AF) class is mostly seen during SBLs (43%) and NNBLs (40%). Overall atmospheric fronts (AF) have a minimum of 17% for unstable, near-neutral, and stable states. This is consistent with a visual inspection of the atmospheric front images where NV, WS, or MC could be present on either side of the front.

The WS images have at least 10% in each of the 3 MABL states suggesting that both upward and downward buoyancy flux can exist for these strong shear production cases [34]. The majority (72%) of the roll (WS) images have *Ri* that are close to zero corresponding to NNBLs. Lastly, WS/MC and MC images are mostly unstable ( $> 72\%$ ).

Figure 4a shows the relationship between the SAR image classification and virtual air-sea temperature difference ( $\Delta T_v$ ) and 10-m wind speed ( $U10$ ). The results are similar to Woodcock [39] who identified cell (MC) and roll (WS)-like circulations from the soaring behavior of birds far offshore. The WS/MC and MC classes mostly have negative  $\Delta T_v$  ( $> 93\%$ ), meaning there is upward buoyancy. These images have the largest range of temperature differences spanning  $-15^\circ\text{C}$  to  $+2^\circ\text{C}$ . WS and atmospheric front (AF) images have positive (43%) and negative (57%)  $\Delta T_v$  consistent with previous work [10, 34]. The majority of cases (63%) are between  $-3$  to  $+3$   $^\circ\text{C}$   $\Delta T_v$  and  $U10 \geq 5$   $\text{m s}^{-1}$

consistent with MABL rolls being associated with shear instability [34, 40–42]. The rolls (WS) have the strongest wind speeds including three events exceeding  $15$   $\text{m s}^{-1}$ . In the  $\Delta T_v$  regime where either WS or WS/MC are found, rolls (WS) are associated with notably stronger wind speeds.

The high correlation between SAR image texture and *Ri* indicates that stratification is a leading controlling parameter for MABL coherent structure variation and that SAR is an effective gauge of MABL stratification. The majority ( $> 91\%$ ) of the internal waves (IW), NV, and AW images have positive  $\Delta T_v$  (upward buoyancy flux). These three SAR image classes mostly occur at wind speeds of  $2$  to  $10$   $\text{m s}^{-1}$  (96%). Borvaran et al., [18] show a similar plot of  $\Delta T$  vs  $U10$  (their Figure 10) using observations from the Air-Sea Interaction Tower (ASIT). The black oval in Figure 4a indicates the high wind shear data location highlighted in Borvaran et al., [18], where their observed vertical wind shear ( $\frac{\Delta U}{\Delta z}$ ) exceeded  $0.05$   $\text{m s}^{-1} \text{m}^{-1}$ . The SBLs (IW, NV, and AW classes) are most common in this region implying that these SAR-observed cases correspond to large vertical shears which are critical for energy production and turbine loads induced by the asymmetric vertical forces on the blades [43–45].

These results emphasize that buoyancy alone is not as good a predictor of the MABL state since stratification quantifies the relative contributions of buoyancy and shear. Changes in the character of the MABL flow, such as evidenced by changes in the characteristic coherent structures, occur at thresholds that mark transitions in the relative contributions of these competing leading order forcing terms. Figure 4b shows the same dataset now plotted versus *Ri* and  $U10$ . Competition between forcing terms is conventionally measured by nondimensional numbers such as *Ri*. Piece-wise linear regression is objectively fit to the data [46]. The buoy  $U10$  shows a transition or change in slope when rolls emerge for both the negative and positive *Ri* regimes—the presence of yellow stars in Figure 4b. This is likely consistent with critical *Ri* that separates the interquartile ranges of the roll (WS) class and the cell (WS/MC or MC) classes in Table 2 and is roughly around  $-0.010$  and  $+0.011$ . There is considerable scatter in the data and piece-wise fit only explains 54% ( $R^2 = 0.54$ ) of the variance. Further investigation of the critical *Ri* between pure rolls (WS) and forced



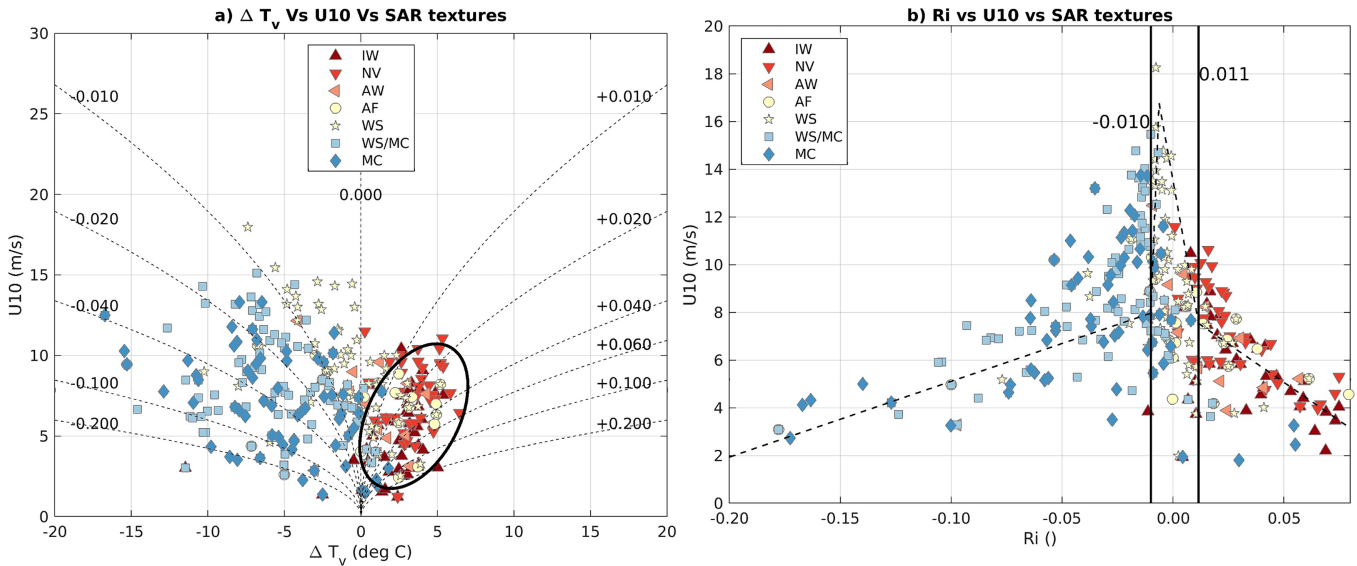


**FIGURE 4** | (a) SAR textures related to the buoy measurements of air-sea virtual temperature difference,  $\Delta T_v$ , a proxy for buoyancy, and  $U_{10}$ , a proxy for shear. The dashed contours are the bulk Richardson number ( $Ri$ ). The black oval refers to the cases that are expected to have strong vertical wind shear ( $\frac{\Delta U}{\Delta z}$ ) based on the LiDAR measurements described in Borvaran et. al., [18]. (b) SAR textures related to the  $Ri$  and  $U_{10}$ . The dashed lines are piece-wise linear fit to the data. The vertical lines denote the intersections of the dashed lines and represent the transitions between unstable/near-neutral and near-neutral/stable MABL states. The markers denote the seven different SAR classes (IW, NV, AW, AF, WS, WS/MC, MC), and the colors (red, yellow, and blue) represent the stable, near-neutral, and unstable states, respectively.

convective states (WS/MC) or pure rolls (WS) and stable states (NV) is needed. If these critical Richardson numbers note the transitions between stable and near-neutral and near-neutral and unstable hold, they could constrain air-sea flux parameterizations and operational models.

In summary, the SAR textures map with reasonable precision to different stratification regimes measured at the buoy. NV, AW, and internal waves (IW) SAR textures correlate to SBLs and likely correspond with significant vertical wind shear. Rolls (WS) and atmospheric fronts (AF) SAR textures correspond to NNBLs, and shear plays an important role. Lastly, force convective (WS/MC and MC) cases correspond to UBLs and strongly depend on buoyancy.

### 3.2 | Atmospheric Stratification Climatology

The above results only pertain to the 420 SAR images that matched the buoy, and the conditions were relatively consistent for the preceding 3 h of the SAR overpass. This section documents the climatology of the seasonal stratification relative to the full 627 images after removing the undefined images. Figure 5a shows the seasonal wind speed and stratification from the buoy and SAR. The monthly average  $U_{10N}$  exceeds  $7 \text{ m s}^{-1}$  for 6 months of the year. The highest SAR wind speeds derived from CMOD5N occur in December–January–February (DJF) ( $9.4, 9.3, 9.1 \text{ m s}^{-1}$ ) and the lowest in June–July–August (JJA) ( $5.7, 4.8, 4.7$ ). The SAR wind speeds have a negative bias from November to June and a positive bias from July to October relative to the CPA observations.  $\Delta T_v$  also has seasonal variations with negative and positive values in DJF and JJA, respectively.

Figure 5b,c shows the seasonal averages of the  $\sim 7$ -year buoy time series ( $N \approx 10^6$ ) relative to the sparse hand-labeled S-1 dataset

( $N = 627$ ). The buoy classification of the MABL state is based on the  $Ri$  ranges while the SAR classification is based on the image textures. The annual average occurrences of  $Ri > 0.12$ /stable are 38%/32%,  $-0.010 \leq Ri \leq 0.011$ /near-neutral are 27%/29%, and  $Ri < -0.010$ /unstable are 35%/39% for the buoy observations and SAR, respectively. DJF has the largest occurrences of UBLs while JJA is dominated by SBLs. The NNBLs are consistent throughout the year, and they occur 28% of each quarterly season. The transition seasons of March–April–May (MAM) and September–October–November (SON) have higher occurrences of NNBLs. The percentages of the SAR textures or the MABL states based on  $Ri$  are similar between the two observational techniques; however, there are differences. For example, in JJA, SAR estimates SBLs occur 58% of the time compared to the buoy's 75%. The nearby study using the Cape wind tower by [16] noted that this region is most likely to have a seasonal maximum of SBLs in MAM. Our study area is located further from land, and we find a higher occurrence of stable conditions in JJA. This difference might be related to climatological differences between the near-land tower and the buoy location 143 km away.

Stratification is strongly related to the wind direction. SBLs typically correspond to warm advection (south to north flow), and UBLs correspond to cold advection (north to south flow). Figure 6 shows the relationship between occurrences, wind direction, and MABL state for the buoy and SAR observations in DJF and JJA. In DJF, unstable boundary dominate because NW wind tends to advect cooler air south to warmer water, making the stratification more unstable and consequently tend to increase occurrences of forced convective states (WS/MC and MC). The buoy and SAR wind direction from  $\approx 310^\circ$  matches. During JJA, the southerly flow is common because of synoptic high-pressure systems. Southerly flow ( $135^\circ$ – $260^\circ$ ) advects warm air north, which tends to increase the stratification and consequently suppresses cells (MC). Independent of the season,

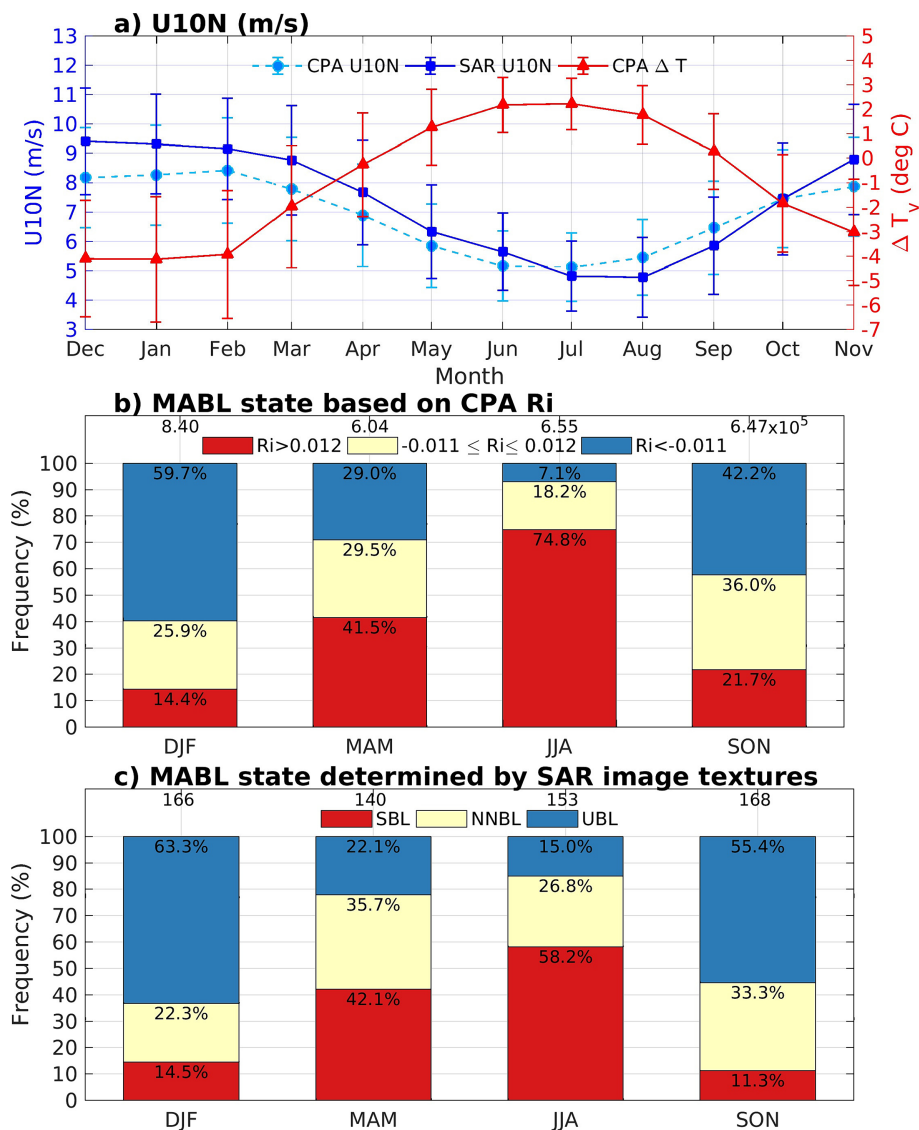


**FIGURE 5** | (a) Monthly median wind speed at 10-m elevation measured at the buoy and derived from SAR using CMOD5N (dots) and monthly median  $\Delta T_v$  from the buoy (triangles). The error bars represent one standard deviation of the monthly data. (b) Seasonal atmospheric stratification is classified using the measured buoy  $Ri$  where the colors represent the  $Ri$  regime. (c) Seasonal atmospheric stratification based on the SAR image textures. The percentages are given on the bars and the number of observations is given at the top of panels (b) and (c).

SBLs are most commonly associated with warm advection. Conversely, UBLs more commonly occur with cold advection. However, there are instances, where SBLs coincide with wind directions from the north and UBLs coincide with wind directions from the south. The 3 categories of SAR states representing stable (IW, NV, and AW), near-neutral (AF and WS), and unstable (WS/MC and MC) boundary layers capture the same features as the buoy despite the fewer samples in the SAR dataset.

The buoy location is positioned to capture the dynamics surrounding the continental shelf break where the Gulf Stream modulates the ocean conditions. We observed many SAR images with oceanographic signatures. Indeed, 27% of the archive contains internal waves (IW) or OF. Despite these frequent ocean signatures, the lack of atmospheric signatures, especially in the internal wave (IW) class, still gives meaningful information about the MABL state. In other words, ocean features are more visible in the SAR

ocean surface roughness with the atmosphere lacking strong rolls or cells. The two technologies, a moored buoy, and a satellite, complement themselves. SAR captures an instantaneous measure of the atmospheric stratification over its footprint while the buoy records a time history. This limited SAR texture dataset of 704 images can characterize the seasonal stratification relative to the ample buoy time series. Previous studies [47, 48] analyzed the satellite sampling needed to define wind speed probability distributions. These studies determined that 100 observations could resolve the mean state consistent with our findings that  $\approx 700$  images resolved the mean boundary layer state.

#### 4 | Discussion

Previous work demonstrated that SAR images with an automated image classification system can identify the boundary

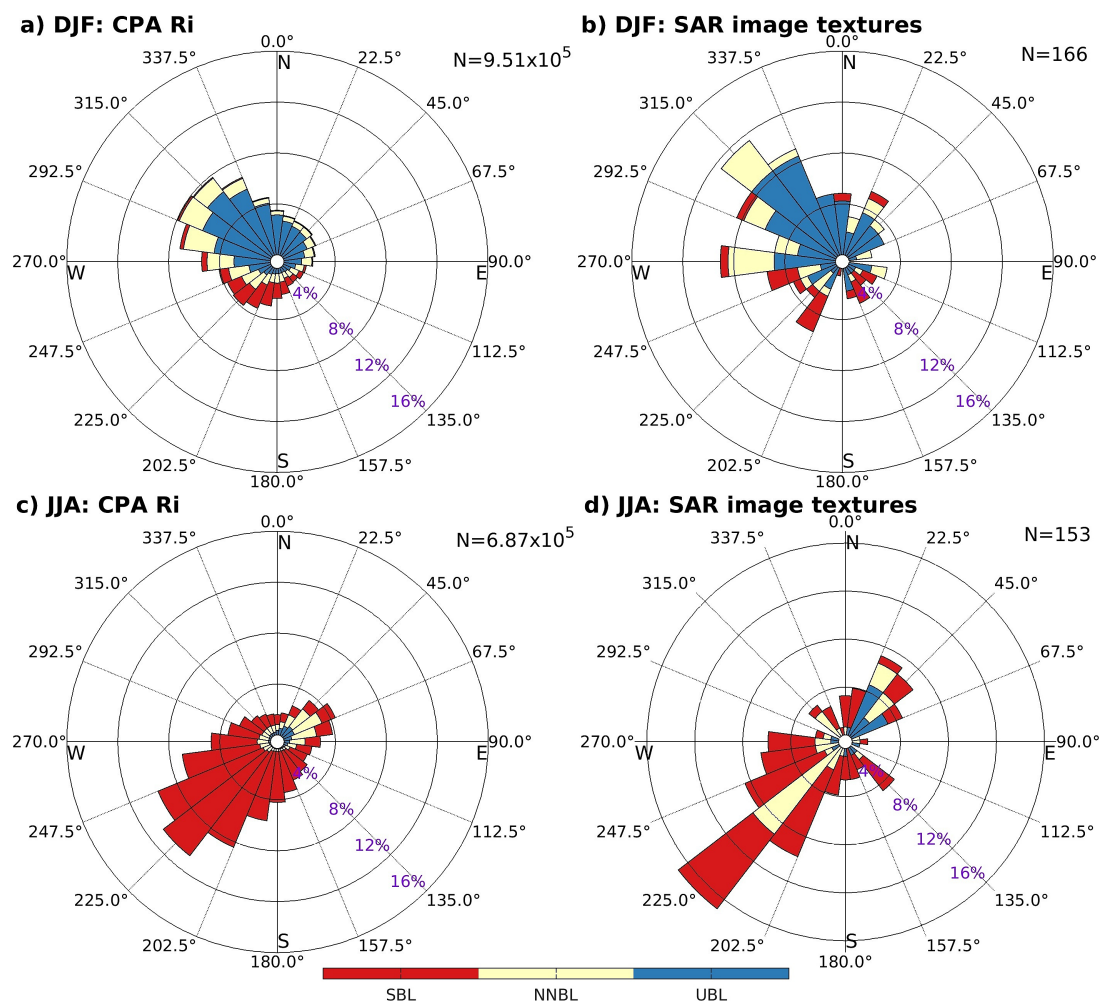


**FIGURE 6** | Wind directional frequency distribution of stratification MABL state based on  $Ri$  from the buoy in (a) DJF and (c) JJA for 2014–2022 where the colors represent the MABL state. The bottom panels show the wind directional frequency distribution of SAR textures. The wind direction is from ERA5 for (b) DJF and (d) JJA for 2014–2022 where the colors are based on the SAR textures. The number of observations is given in the top right of each panel.

layer states [10]. These results were based on the global statistics referencing an ERA5-derived Richardson number. In this work, we show that the lack of rolls or cells (NV), rolls (WS), and cells (MC) correspond to stable (+  $Ri$ ), near-neutral ( $\pm Ri$ ), and unstable ( $- Ri$ ) boundary layer states (e.g. Figure 3) relative to buoy observations. Additionally, the S-1 WV can provide a regional seasonal climatology of atmospheric states and is consistent with nearby buoy measurements from the CPA (e.g., Figures 5 and 6). The large SAR database of S-1 WV can likely resolve the seasonal cycle of MABL stratification states in other locations worldwide. The WV has near-global coverage. However, coastal regions can also utilize the wide swath imaging modes of S-1 similar to [49]. A synergistic approach using multiple satellite technologies benefits wind energy site characterization [50]. The results of this work show that SAR provides information about atmospheric stratification helping to fill the data gap laid out by Shaw et al. [1].

A new finding that might be somewhat specific to this region is the ability of SAR to capture many occasions of SBL conditions. Nearby studies based on observations show that the wind speed profile is often nonlogarithmic and high turbulent kinetic energy is associated with SBLs [16, 18]. A recent nearby LiDAR-based

study by [18] showed that strong vertical wind shear at wind turbine heights of 80 m is common for SBLs. Figure 4 in this work shows the highlighted region of [18] corresponds to SBLs. Given the importance of stable conditions to offshore wind resource siting, energy production [51], system design, fatigue [43, 52, 53], and operations, the SAR method of using the lack of rolls and cells to designate SBLs could be used to estimate regional climatologies of MABL states for the offshore wind community. The lack of atmospheric signatures (NV class) corresponds to SBL and images with ocean features like internal gravity waves (IW) also correspond to SBLs. This more acute finding might not hold in other regions and future studies can determine if internal waves are observed in SAR imagery when the atmosphere is stably stratified.

Figure 4b shows that the buoy wind speed shows a transition or change in slope when rolls emerge for both the negative and positive  $Ri$  regimes (the presence of yellow star markers). The transitions are consistent with the  $Ri$  that separate the inter-quartile ranges of the roll (WS) class and the cell (WS/MC or MC) classes in Table 2 and is roughly around  $-0.010$ . For positive  $Ri$ , the wind speed transition is not as clear, but there seems to be an inflection near 0.011. These values were determined by an objective multiple linear piecewise fit and by averaging the interquartile



ranges in Table 2 lower and upper boundaries between unstable, near-neutral, and stable boundary layers. There are large variations in the datasets so further investigation is warranted. Some of the variability might be related to the large spatial differences between buoy and SAR images. The SAR textures are an absolute indicator of the boundary layer state and when combined with in situ observations, it is a powerful technique to understand the MABL physics of air-sea fluxes. The two transitions  $Ri$  numbers of  $-0.01$  and  $0.011$  represent the transition between unstable/near-neutral and near-neutral/stable regimes, respectively. If these critical  $Ri$  hold, they could constrain air-sea flux parameterizations and operational models.

In the offshore wind community, it is common practice to deploy floating LiDAR systems to accurately characterize the boundary layer by estimating the wind speeds at the hub heights and turbulent kinetic energy. LiDAR systems are expensive and take considerable effort to maintain. Our method of using SAR textures to characterize the boundary layer stratification is a less expensive option and a climatology can be completed before an offshore wind site is leased. The open data policy of S-1 and global coverage makes it possible to estimate the stratification climatologies at regional scales. Furthermore, remote sensing tools offer the possibility of describing spatial variability, which is advantageous to siting numerous offshore wind farm locations. The SAR texture information complements the high-resolution coastal climatologies from SAR [2, 48, 49].

SAR has been used for wind energy assessment and monitoring applications mainly for site characterization due to its high resolution [2–5] and can even resolve wakes generated by turbines [6]. Recent works related SAR sea surface roughness to wind speeds at turbine heights ( $\approx 80$  m) [7–9]. In this work, we demonstrate SAR can also characterize the stratification climate by using a three-state classification: cells, rolls, or lack of them corresponding with unstable, near-neutral, and stable stratification regimes (Figures 3 and 4). Future wind energy site assessments can be complemented by using SAR images to estimate the stratification, especially in regions that lack observations such as the regions offshore of the east coast of South America currently being considered for offshore wind development. With the onset of commercial SAR satellite systems such as Capella, ICEYE, PredaSAR, or Umbra, there is a possible future enterprise of characterizing remote locations that lack in-situ observations.

## 5 | Conclusion

Offshore wind development is expected to greatly increase in the coming decades because of the reduction in capital and operating costs: 17%–35% reduction by 2035 and 37%–49% reduction by 2050 due to bigger and more efficient turbines [54]. Previous research showed inadequacies in datasets to describe the atmospheric stratification and near-surface mean state in offshore ocean environments [1, 23]. This study demonstrates that this observation data gap can be addressed by using SAR imagery to infer information about atmospheric stratification. The method used here is based on a by-eye classification of 704 S-1 C-band SAR images in the NW Atlantic, an area of rapid offshore wind development. There is a strong relationship between the SAR-observed ocean surface textures and stratification regimes measured in situ using

a bulk Richardson number ( $Ri$ ). The satellite/buoy matches show that 96% of the forced convective cases (WS/MC and MC) occur when  $Ri < 0$  corresponding to UBLs, rolls (WS) reside in a narrow  $Ri$  range centered near  $-0.005$  corresponding to NNBLs, and 95% of images lacking rolls (WS) or cells (MC) (namely, the IW, NV, and AW SAR classes) occur when  $Ri > 0$  corresponding to SBLs. Thus, the SAR textures accurately distinguish between positive and negative air-sea temperature differences.

Remotely sensed surface winds from SAR have previously been used for offshore wind resources and turbine wake assessment [3, 5, 6, 49]. In this work, we show that SAR gives additional information about MABL stratification that, in turn, indicates vertical wind shear characteristics; important information for both the production from [51] and operation of turbines [52]. From a site offshore wind assessment perspective, it is notable that SAR systems are unaffected by clouds and operate in all weather conditions. Several private companies provide custom SAR data collection that can be used for site assessment and monitoring. Automated SAR scene classification methods like the image detection algorithms of [55] can describe stratification for any location [10]. The SAR detection capability suggests that atmospheric stratification and identifying the critical stable conditions can be determined from space using the nearly untapped SAR images for wind energy assessments and monitoring.

## Author Contributions

**Justin E. Stopa, Doug Vandemark, and Ralph Foster:** conceptualization. **Justin E. Stopa, Doug Vandemark, and Marc Emond:** data curation. **Justin E. Stopa:** formal analysis. **Ralph Foster, Justin E. Stopa, and Doug Vandemark:** funding acquisition. **Justin E. Stopa, Doug Vandemark, and Ralph Foster:** investigation. **Justin E. Stopa, Doug Vandemark, Ralph Foster, Alexis Mouche, and Bertrand Chapron:** methodology.

## Acknowledgments

R.F. and D.V. were supported by NASA Physical Oceanography through grants NNX17AH17G and 80NSSC20K0822. The latter NASA grant, 80NSSC20K0822, and grant number 2132150 from the National Science Foundation supported J.S. and is referenced by the School of Ocean and Earth Science and Technology (SOEST) contribution number 11822. A.M. was supported by ESA Contract No. 4000135827/21/NL - Harmony Science Data Utilisation and Impact Study for Ocean. A.M. and B.C. were also supported by ESA Sentinel-1 Mission Performance Center 465 (4000107360/12/I-LG). We thank ESA for providing the data and IFREMER for the computing resources used in this study. This material is based on work supported by the Ocean Observatories Initiative (OOI), a major facility fully funded by the National Science Foundation under Cooperative Agreement No. 1743430, and the Woods Hole Oceanographic Institution OOI Program Office.

## Conflicts of Interest

The authors declare no conflicts of interest.

## Data Availability Statement

All SAR Wave Mode images are freely available at ESA's Sentinel Open Access Hub (<https://sentinel.esa.int/web/sentinel/sentinel-data-access>) and also the Alaska Satellite Facility (<https://asf.alaska.edu/data-sets/sar-data-sets/sentinel-1/sentinel-1-data-and-imagery/>). The near-surface parameters from the OOI are accessible through [https://ooinet.oceanobservatories.org/data\\_access/?search=CP01CNSM-SBD11-06-METBKA00](https://ooinet.oceanobservatories.org/data_access/?search=CP01CNSM-SBD11-06-METBKA00).

## References

1. W. J. Shaw, L. K. Berg, M. Debnath, et al., "Scientific Challenges to Characterizing the Wind Resource in the Marine Atmospheric Boundary Layer," *Wind Energy Science* 7, no. 6 (2022): 2307-2334.
2. C. B. Hasager, M. Badger, A. Peña, X. G. Larsén, and F. Bingöl, "SAR-Based Wind Resource Statistics in the Baltic Sea," *Remote Sensing* 3, no. 1 (2011): 117-144.
3. C. Hasager, P. Vincent, J. Badger, et al., "Using Satellite SAR to Characterize the Wind Flow Around Offshore Wind Farms," *Energies* 8, no. 6 (2015): 5413-5439.
4. C. B. Hasager, A. Mouche, M. Badger, et al., "Offshore Wind Climatology Based on Synergetic Use of Envisat ASAR, ASCAT and QuikSCAT," *Remote Sensing of Environment* 156 (2015): 247-263.
5. B. Djath, J. Schulz-Stellenfleth, and B. Cañadillas, "Study of Coastal Effects Relevant for Offshore Wind Energy Using Spaceborne Synthetic Aperture Radar (SAR)," *Remote Sensing* 14, no. 7 (2022): 1688.
6. B. Djath, J. Schulz-Stellenfleth, and B. Cañadillas, "Impact of Atmospheric Stability on X-Band and C-Band Synthetic Aperture Radar Imagery of Offshore Windpark Wakes," *Journal of Renewable and Sustainable Energy* 10, no. 4 (2018): 43301.
7. T. Ahsbahs, M. Badger, I. Karagali, and X. Larsén, "Validation of Sentinel-1A SAR Coastal Wind Speeds Against Scanning LiDAR," *Remote Sensing* 9, no. 6 (2017): 552.
8. M. Badger, T. Ahsbahs, P. Maule, and I. Karagali, "Inter-Calibration of SAR Data Series for Offshore Wind Resource Assessment," *Remote Sensing of Environment* 232 (2019): 111316.
9. L. de Montera, H. Berger, R. Husson, P. Appelghem, L. Guerlou, and M. Fragoso, "High-Resolution Offshore Wind Resource Assessment at Turbine Hub Height With Sentinel-1 SAR Data and Machine Learning," *Wind Energy Science* 7, no. 4 (2022): 1441-1453.
10. J. E. Stopa, C. Wang, D. Vandemark, R. C. Foster, A. Mouche, and B. Chapron, "Automated Global Classification of Surface Layer Stratification Using High-Resolution Sea Surface Roughness Measurements by Satellite Synthetic Aperture Radar," *Geophysical Research Letters* 49, no. 12 (2022): e2022GL098686.
11. T. D. Sikora, G. S. Young, H. N. Shirer, and R. D. Chapman, "Estimating Convective Atmospheric Boundary Layer Depth From Microwave Radar Imagery of the Sea Surface," *Journal of Applied Meteorology* 36, no. 7 (1997): 833-845.
12. T. D. Sikora, G. S. Young, C. M. Fisher, and M. D. Stepp, "A Synthetic Aperture Radar-Based Climatology of Open-Cell Convection Over the Northeast Pacific Ocean," *Journal of Applied Meteorology and Climatology* 50, no. 3 (2011): 594-603.
13. R. C. Foster, "Why Rolls Are Prevalent in the Hurricane Boundary Layer," *Journal of the Atmospheric Sciences* 62, no. 8 (2005): 2647-2661.
14. A. A. Grachev, and C. W. Fairall, "Dependence of the Monin-Obukhov Stability Parameter on the Bulk Richardson Number Over the Ocean," *Journal of Applied Meteorology* 36, no. 4 (1997): 406-414.
15. H. Hersbach, B. Bell, P. Berrisford, et al., "The Era5 Global Reanalysis," *Quarterly Journal of the Royal Meteorological Society* 146, no. 730 (2020): 1999-2049.
16. C. L. Archer, B. A. Colle, D. L. Veron, F. Veron, and M. J. Sienkiewicz, "On the Predominance of Unstable Atmospheric Conditions in the Marine Boundary Layer Offshore of the U.S. Northeastern Coast," *Journal of Geophysical Research: Atmospheres* 121, no. 15 (2016): 8869-8885.
17. N. Bodini, J. K. Lundquist, and A. Kirincich, "U.S. East Coast Lidar Measurements Show Offshore Wind Turbines Will Encounter Very Low Atmospheric Turbulence," *Geophysical Research Letters* 46, no. 10 (2019): 5582-5591.
18. D. Borvarán, A. Peña, and R. Gandoin, "Characterization of Offshore Vertical Wind Shear Conditions in Southern New England," *Wind Energy* 24, no. 5 (2020): 465-480.
19. W. Musial, P. Spitsen, P. Beiter, et al., "Offshore Wind Market Report: 2021 Edition," tech. rep. (U.S. Department of Energy - Office of Energy Efficiency and Renewable Energy, 2021).
20. NSF Ocean Observatories Initiative. "Bulk Meteorology Instrument Package (METBKA) Data the Coastal Pioneer New England Shelf Array From 21 November 2013, 18:16:23Z to 11 November 2022, 13:20:35Z. CP01CNSM-SBD11-06-METBKA000," (2024), accessed January 10, 2023, [https://ooinet.oceanobservatories.org/data\\_access/?search=CP01CNSM-SBD11-06-METBKA000](https://ooinet.oceanobservatories.org/data_access/?search=CP01CNSM-SBD11-06-METBKA000).
21. C. R. Jackson, J. R. Apel, P. Clemente-Colón, W. G. Pichel, R. A. Shuchman, and C. C. Wackerman, "Synthetic Aperture Radarmarine User's Manual," tech. rep. (National Oceanic and Atmospheric Administration, 2004).
22. C. Wang, A. Mouche, P. Tandeo, et al., "A Labelled Ocean Sar Imagery Dataset of Ten Geophysical Phenomena From Sentinel-1 Wave Mode," *Geoscience Data Journal* 6, no. 2 (2019): 105-115.
23. S. C. Pryor, and R. J. Barthelmie, "A Global Assessment of Extreme Wind Speeds for Wind Energy Applications," *Nature Energy* 6, no. 3 (2021): 268-276.
24. J. B. Edson, V. Jampana, R. A. Weller, et al., "On the Exchange of Momentum Over the Open Ocean," *Journal of Physical Oceanography* 43, no. 8 (2013): 1589-1610.
25. H. Hersbach, "Comparison of C-Band Scatterometer CMOD5.n Equivalent Neutral Winds With ECMWF," *Journal of Atmospheric and Oceanic Technology* 27, no. 4 (2010): 721-736.
26. W. Koch, "Directional Analysis of SAR Images Aiming at Wind Direction," *IEEE Transactions on Geoscience and Remote Sensing* 42, no. 4 (2004): 702-710.
27. T. D. Sikora, G. S. Young, R. C. Beal, and J. B. Edson, "Use of Spaceborne Synthetic Aperture Radar Imagery of the Sea Surface in Detecting the Presence and Structure of the Convective Marine Atmospheric Boundary Layer," *Monthly Weather Review* 123, no. 12 (1995): 3623-3632.
28. P. D. Mourad, and B. A. Walter, "Viewing a Cold Air Outbreak Using Satellite-Based Synthetic Aperture Radar and Advanced Very High Resolution Radiometer Imagery," *Journal of Geophysical Research: Oceans* 101, no. C7 (1996): 16391-16400.
29. G. Levy, "Boundary Layer Roll Statistics From SAR," *Geophysical Research Letters* 28, no. 10 (2001): 1993-1995.
30. G. S. Young, T. D. Sikora, and N. S. Winstead, "Use of Synthetic Aperture Radar in Finescale Surface Analysis of Synoptic-scale Fronts at Sea," *Weather and Forecasting* 20, no. 3 (2005): 311-327.
31. M. A. LeMone, "The Structure and Dynamics of Horizontal Roll Vortices in the Planetary Boundary Layer," *Journal of the Atmospheric Sciences* 30, no. 6 (1973): 1077-1091.
32. T. M. Weckwerth, T. W. Horst, and J. W. Wilson, "An Observational Study of the Evolution of Horizontal Convective Rolls," *Monthly Weather Review* 127, no. 9 (1999): 2160-2179.
33. S. R. Santellanes, G. S. Young, D. J. Stensrud, M. R. Kumjian, and Y. Pan, "Environmental Conditions Associated With Horizontal Convective Rolls, Cellular Convection, and No Organized Circulations," *Monthly Weather Review* 149, no. 5 (2021): 1305-1316.
34. R. A. Brown, "On the Inflection Point Instability of a Stratified Ekman Boundary Layer," *Journal of the Atmospheric Sciences* 29, no. 5 (1972): 850-859.
35. R. L. Grossman, "An Analysis of Vertical Velocity Spectra Obtained in the Bomex Fair-Weather, Trade-Wind Boundary Layer," *Boundary-Layer Meteorology* 23, no. 3 (1982): 323-357.

36. T. D. Sikora, and D. R. Thompson, "Air-Sea Turbulence Statistics From Synthetic Aperture Radar: An Update," *Canadian Journal of Remote Sensing* 28, no. 3 (2002): 517-523.
37. C. Wang, D. Vandemark, A. Mouche, B. Chapron, H. Li, and R. C. Foster, "An Assessment of Marine Atmospheric Boundary Layer Roll Detection Using Sentinel-1 SAR Data," *Remote Sensing of Environment* 250 (2020): 112031.
38. D. Etling, and R. A. Brown, "Roll Vortices in the Planetary Boundary Layer: A Review," *Boundary-Layer Meteorology* 65, no. 3 (1993): 215-248.
39. A. H. Woodcock, "Convection and Soaring Over the Open Sea," *Journal of Marine Research* 3 (1940): 248-253.
40. A. J. Faller, "Large Eddies in the Atmospheric Boundary Layer and Their Possible Role in the Formation of Cloud Rows," *Journal of the Atmospheric Sciences* 22, no. 2 (1965): 176-184.
41. D. K. Lilly, "On the Instability of Ekman Boundary Flow," *Journal of the Atmospheric Sciences* 23, no. 5 (1966): 481-494.
42. R. A. Brown, "A Secondary Flow Model for the Planetary Boundary Layer," *Journal of the Atmospheric Sciences* 27, no. 5 (1970): 742-757.
43. A. J. Eggers, R. Digumarthi, and K. Chaney, "Wind Shear and Turbulence Effects on Rotor Fatigue and Loads Control," *Journal of Solar Energy Engineering* 125, no. 4 (2003): 402-409.
44. C. G. Nunalee, and S. Basu, "Mesoscale Modeling of Coastal Low-level Jets: Implications for Offshore Wind Resource Estimation," *Wind Energy* 17, no. 8 (2013): 1199-1216.
45. Y. L. Pichugina, W. A. Brewer, R. M. Banta, et al., "Properties of the Offshore Low Level Jet and Rotor Layer Wind Shear as Measured by Scanning Doppler Lidar," *Wind Energy* 20, no. 6 (2016): 987-1002.
46. R. S. Bogartz, "A Least Squares Method for Fitting Intercepting Line Segments to a Set of Data Points," *Psychological Bulletin* 70, no. 6, Pt.1 (1968): 749-755.
47. R. J. Barthelmie, and S. C. Pryor, "Can Satellite Sampling of Offshore Wind Speeds Realistically Represent Wind Speed Distributions?," *Journal of Applied Meteorology* 42, no. 1 (2003): 83-94.
48. S. C. Pryor, M. Nielsen, R. J. Barthelmie, and J. Mann, "Can Satellite Sampling of Offshore Wind Speeds Realistically Represent Wind Speed Distributions? Part II: Quantifying Uncertainties Associated With Distribution Fitting Methods," *Journal of Applied Meteorology* 43, no. 5 (2004): 739-750.
49. T. Ahsbahs, G. Maclaurin, C. Draxl, C. R. Jackson, F. Monaldo, and M. Badger, "US East Coast Synthetic Aperture Radar Wind Atlas for Offshore Wind Energy," *Wind Energy Science* 5, no. 3 (2020): 1191-1210.
50. M. M. Nezhad, A. Heydari, E. Pirshayan, D. Groppi, and D. A. Garcia, "A Novel Forecasting Model for Wind Speed Assessment Using Sentinel Family Satellites Images and Machine Learning Method," *Renewable Energy* 179 (2021): 2198-2211.
51. E. L. Petersen, N. G. Mortensen, L. Landberg, J. Højstrup, and H. P. Frank, "Wind Power Meteorology. Part I: Climate and Turbulence," *Wind Energy* 1, no. 1 (1998): 2-22.
52. A. Sathe, J. Mann, T. Barlas, W. A. A. M. Bierbooms, G. J. W. van Bussel, "Influence of Atmospheric Stability on Wind Turbine Loads," *Wind Energy* 16, no. 7 (2012): 1013-1032.
53. Y. Guo, J. Keller, and W. LaCava, "Planetary Gear Load Sharing of Wind Turbine Drivetrains Subjected to Non-Torque Loads," *Wind Energy* 18, no. 4 (2014): 757-768.
54. R. Wiser, J. Rand, J. Seel, et al., "Expert Elicitation Survey Predicts 37% to 49% Declines in Wind Energy Costs by 2050," *Nature Energy* 6, no. 5 (2021): 555-565.
55. C. Wang, P. Tando, A. Mouche, et al., "Classification of the Global Sentinel-1 SAR Vignettes for Ocean Surface Process Studies," *Remote Sensing of Environment* 234 (2019): 111457.